

Andrzej Chybicki\* and Zbigniew Łubniewski

# Optimized AVHRR land surface temperature downscaling method for local scale observations: case study for the coastal area of the Gulf of Gdańsk

Received October 25, 2016; accepted June 1, 2017

**Abstract:** Satellite imaging systems have known limitations regarding their spatial and temporal resolution. The approaches based on subpixel mapping of the Earth's environment, which rely on combining the data retrieved from sensors of higher temporal and lower spatial resolution with the data characterized by lower temporal but higher spatial resolution, are of considerable interest. The paper presents the downscaling process of the land surface temperature (LST) derived from low resolution imagery acquired by the Advanced Very High Resolution Radiometer (AVHRR), using the inverse technique. The effective emissivity derived from another data source is used as a quantity describing thermal properties of the terrain in higher resolution, and allows the downsampling of low spatial resolution LST images. The authors propose an optimized downscaling method formulated as the inverse problem and show that the proposed approach yields better results than the use of other downsampling methods. The proposed method aims to find estimation of high spatial resolution LST data by minimizing the global error of the downscaling. In particular, for the investigated region of the Gulf of Gdańsk, the RMSE between the AVHRR image downsampled by the proposed method and the Landsat 8 LST reference image was  $2.255^{\circ}\text{C}$  with correlation coefficient  $R$  equal to 0.828 and Bias =  $0.557^{\circ}\text{C}$ . For comparison, using the PBIM method, it was obtained RMSE =  $2.832^{\circ}\text{C}$ ,  $R = 0.775$  and Bias =  $0.997^{\circ}\text{C}$  for the same satellite scene. It also has been shown that the obtained results are also good in local scale and can be used for areas much smaller than the entire satellite imagery scene, depicting diverse biophysical conditions. Specifically, for the analyzed set of small sub-datasets of the whole scene, the obtained RSME between the downsampled and reference image was smaller, by approx.  $0.53^{\circ}\text{C}$  on average, in the case of applying the proposed method than in the case of using the PBIM method.

**Keywords:** inverse problem, LST, Landsat, AVHRR, downscaling, multi-resolution, Tikhonov regularization, Gulf of Gdańsk

## 1 Introduction

Remote multispectral sensing is an important tool for environment monitoring that has several applications in industry and science. Particularly, satellite thermal-infrared observations (TIR) are of high importance as they allow for observing and analyzing several physical and other phenomena that take place in the Earth's environment, namely air-soil heat fluxes, atmospheric processes and vegetation changes, radiation processes, evapotranspiration and other phenomena in global, regional and local scales.

When taking the data quality and its applications into account, several criteria can be considered, such as spatial resolution, time resolution (the revisit time), data accuracy, spectral resolution, etc. Due to technical constraints, it may be said that each Earth observation satellite system is a kind of a compromise between several criteria mentioned above. In order to reduce the drawbacks of low quality of a particular sensor in one aspect, other sensors can fill the gap in another aspect in order to provide the most comprehensive overview on the Earth's environment. Thus, low spatial resolution meteorological satellites provide global information on the state of the atmosphere and are characterized by a relatively short revisit time. Others,

**\*Corresponding Author: Andrzej Chybicki:** Gdańsk University of Technology, Faculty of Electronics, Telecommunication and Informatics, Department of Geoinformatics, Narutowicza 11/12, Gdańsk 80-233, Poland, E-mail: andrzej.chybicki@eti.pg.gda.pl

**Zbigniew Łubniewski:** Gdańsk University of Technology, Faculty of Electronics, Telecommunication and Informatics, Department of Geoinformatics, Narutowicza 11/12, Gdańsk 80-233, Poland

such as LANDSAT or Sentinel-2, are used mainly for high resolution land monitoring. Since the spatial and temporal resolution of TIR imaging systems are negatively correlated, an approach based on subpixel mapping of the Earth's environment is of high interest.

Subpixel mapping relies on combining the data retrieved from sensors at different spatial and time resolution in order to generate products which would combine the advantages of products that they have been generated from. The retrieved datasets are a combination of high spatial resolution imagery with datasets characterized by lower spatial resolution but being more frequently registered. The combination of both sources yields a new quality in observation products because the data is frequently delivered and has higher spatial resolution. As a consequence, this enables the potential use of low resolution thermal datasets in observing phenomena at a higher scale, such as microclimate studies, human activities monitoring, urban heat island effects observations [1], urban and peri-urban areas canopy characterization or local water containers quality monitoring [2, 3]. Moreover, it enables for better understanding of and identifying processes of urban and sub-urban heat balance and better characterization of urban microclimate changes [4].

Despite the long history of available LST generated from space-borne observations, recent activities aiming to remove barriers related to low resolution observations are of considerable interest. There are several approaches in the literature that aim to construct synergistic methods exploiting information from time- and spatial- multiresolution datasets in order to retrieve the sub-scale spatial information about an observed area. For instance, Kustas et al. [5] proposed a coarse resolution temperature disaggregation method based on vegetation indices and surface radiometric temperature validated by a sensing-based energy balance model over US Southern Great Planes. G. Yang [6] proposed a method of imagery downscaling based on endmember function remote sensing indices calculated from the reflectivity data of ASTER VNIR/SWIR wavebands and land cover types database, processed with the genetic algorithm and self-organizing feature map artificial neural network (GA-SOFM-ANN) for heterogeneous area of Changping District, located on the northeast of Beijing City, China. Many approaches are also focused on urban area LST downscaling like M. Stathopoulou [7], who sharpened AVHRR thermal images and derived daily LST of 250-m spatial resolution for four cities in Greece, or Mitraka et al. [8], who focused on urban and suburban areas of Heraklion, Greece. Also, Bechtel et al. [9] downscaled SEVIRI data by a factor of two for monitoring UHI in Hamburg, Germany, while Keramitsoglou et al. [10] tested dif-

ferent regression algorithms for the same purpose over the area of Athens, Greece. Other approaches rely on estimating high resolution features directly by models that have been trained on, or calibrated to training datasets [11–14], or on utilizing soft-classification procedures to estimate the degree of membership of each pixel with respect to each of the end-member classes. Methods that rely on using artificial neural networks [15], fuzzy classifiers [16–18], or Adaptive Subpixel Mapping Based on a Multiagent System [19] can be also found in the literature.

The approach [13] that uses a linear mixture model based on the assumption that the spectral response  $x_k$  of a pixel  $k$  is a linear weighted sum of spectral responses of its component classes expressed by:

$$x_k = M \cdot f + e, \quad (1)$$

where  $M$  is a  $q$  by  $c$  matrix in which  $q$  represents the number of wavebands and  $c$  the number of classes, the term  $f$  represents a vector, of length  $c$ , that expresses the proportional coverage of the classes in the area represented by a pixel, and  $e$  is a term that represents the vector of errors, is to some extent most similar to our methodology. The columns of the matrix  $M$  are end-member spectra, essentially the characteristic spectral responses of the classes.

However, in our study we do not use a set of spectral responses for high resolution pixels, but instead we utilize a sub-sampling kernel retrieved from a high resolution scene that describes quasi-stable radiometric properties of the land surface, namely, the effective emissivity derived from the land cover map type and vegetation index in the form of fractional vegetation cover (FVC). In particular, we assume that estimation of LST high resolution value should be done with taking into account the local effective emissivity high resolution value, but not necessarily with an assumption of the global linear dependency between emissivity and LST like in the PBIM method [20] (subsection 2.2), as suggested by Jiang and Islam [21, 22]. Instead, we introduce and estimate a vector of weights that permits more flexible, and adjusted to local conditions, modeling of dependency between emissivity and LST. This vector of weights is estimated by the so-called inverse downscaling process using the inverse problem approach and utilizing the Tikhonov regularization method.

The proposed algorithm generates a land surface temperature product characterized by high spatial resolution ( $\approx 100$  m) derived from AVHRR imagery, thus having increased revisit frequency. The proposed approach relies on finding an optimal dataset that minimizes differences between the generated downscaled product and original low resolution scene ( $\approx 1.1$  km at nadir). The validation of the process is based on comparing the generated down-



scaled product 100 m high resolution image to Landsat 8 TIRS 100 m LST products registered at the same time. The proposed approach can be applied operationally since the inverse problem approach finds an optimal solution to the problem, in the sense of the mean-square error (MSE). However, operational application of the method requires the prior, detailed analysis of its performance applied on specific region and data, therefore, The proposed algorithms of downscaling were tested and verified for the coastal zone of the Gulf of Gdańsk, Southern Baltic, area of Europe.

Placing the proposed approach in the context of the existing solutions of the mentioned problem, it may be noted that most of the downscaling techniques used utilize a quasi-optimal assumption of dependence between the high resolution kernel (i.e. effective emissivity) and land surface temperature. This dependence is usually computed on the basis of radiative transfer models, is determined empirically or calculated with the use of neural networks [23] or fuzzy logic computing schemes. Because of the issues mentioned above, most of the approaches presented in the literature are not self-adaptive because they require additional information retrieved from external models. What is more, regarding the approaches based on soft computing techniques, like neural networks or fuzzy logic, a computational model used in such cases to calculate the given quantity for fine scale pixels in the course of the downscaling process, is to large extent arbitrary and may not correspond to the physics of the underlying phenomena.

The advantage of the proposed method over the existing approaches is that it finds an optimal solution to the stated problem. In order to present the advantages of the proposed approach, we have compared the obtained results with those achieved using one of the most popular methods - namely the PBIM.

## 2 Problem formulation and solution concept

### 2.1 Downscaling theory

Downscaling is the process of converting a set of spatial information (e.g. 2- or 3-dimensional) from a low to a high resolution. In the context of LST estimation based on satellite imagery, downscaling refers to estimation of LST values within the sub-pixel area. In practice, in order to downscale a satellite image, thus improving its spatial resolution, the approach of merging at least two datasets is used;

a low resolution image is merged to a high resolution image (from the same or different sensor), or a low resolution image obtains spatial details of a high resolution image [24, 25].

According to the downscaling principles, the proposed approach assumes to retain radiometric characteristics of input images and aims to minimize the error. Let us assume two input data sources - such that both sources represent acquisition over the same area, and that a physical quantity they measure is comparable, i.e. they measure the same quantity in the same units (energy, radiance, temperature, etc.). Another point in the methodology is the definition of relation between two data sources that enables transformation from one source domain to another. Both sources have different but spatially constant resolution (Fig. 1).

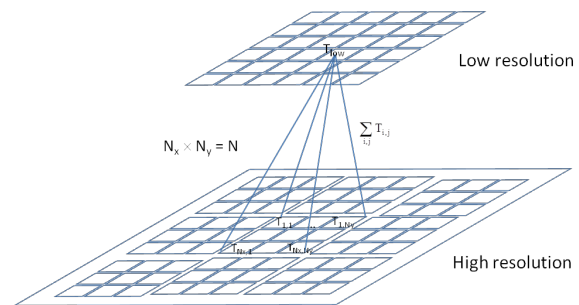


**Figure 1:** Diagram representing the relation between the spatial distribution of measured quantity in high resolution and low resolution

Let us assume that for a given flat area, corresponding to a pixel in coarser resolution, the value of measured quantity is the weighted average of this quantity for all subareas corresponding to pixels in finer resolution contained by the coarse resolution pixel area. It is mathematically expressed as:

$$T_{low} = \sum_{n=1}^N T_{high}^{(n)} \frac{s^{(n)}}{S} \quad (2)$$

where

$$S = \sum_{n=1}^N s^{(n)} \quad (3)$$

where

$T_{low}$  - is the value of the pixel in coarse resolution,  
 $T_{high}^{(n)}$  - is the value of the  $n$ -th pixel in high resolution image belonging to the mentioned high pixel resolution area,  
 $s^{(n)}$  - is the area of the given pixel in high resolution,  
 $S$  - is the area of a single pixel in coarse resolution,  
 $N$  - is the number of pixels in high resolution imagery that

are contained in the corresponding pixel of low resolution image.

In general,  $N$  depends on the ratio of data sources' spatial resolution taken under consideration and may also depend on the number of high resolution pixels being excluded from the analysis for a given low resolution pixel due to cloud presence and other limitations.

The dependency mentioned above enables transformation between the high and low scale. However, as the transformation of pixel values from the high to low scale results in the loss of information, the reverse transformation is obviously ambiguous. The estimation of pixel values of high resolution having given pixel values of low resolution requires some additional, local, high scaled information about characteristics of the specific area that influences the pixel values  $T_{low}$  and  $T_{high}$ , i.e. some independently measured quantity  $Q$  usually derived from satellite imagery or auxiliary database as well. The influence of  $Q$  on  $T$  ought to be stable, which means that the dependence between  $Q$  and  $PV$  should be the same for the entire investigated area. Also,  $Q$  values should be stable in time (to a higher degree than the quantity expressed by  $PV$ ), which makes it easier to collect them (i.e. lower satellite revisit time is needed). In the case of LST as  $T$ , the surface thermal properties expressed by its vegetation index or effective emissivity may be used as  $Q$  [26]. The latter was utilized by the authors in the current study. One of the main assumptions applied is that the generalization of the rule connecting the local emissivity and LST value must be allowed with respect to at least a single scene of low resolution imagery.

The way of utilizing the high resolution information on thermal properties of the land for downscaling the LST image is described in the next subsections.

## 2.2 PBIM method

Having defined the concept of downscaling, let us focus on the particular method of downscaling to be optimized. Since the objective of the study is to present the optimized downscaling AVHRR LST method in view of its applicability in coastal zone LST estimation, we have taken under closer analysis the PBIM (Pixel Block Intensity Modulation) downscaling process, described in the next subsection, and proposed a way of its optimization.

PBIM is proposed for downscaling thermal products to higher resolution using the high resolution transformation kernel. The general form of the PBIM method is expressed

as:

$$T_{high} = \frac{T_{low}\epsilon_{high}}{\epsilon_{high \rightarrow mean}}, \quad (4)$$

where  $T_{low}$  - is the pixel value of the image in low resolution,  $\epsilon_{high}$  - is the high effective emissivity pixel value,  $\epsilon_{high \rightarrow mean}$  - is the high effective emissivity value averaged for a current low resolution pixel area,  $T_{high}$  - is the resulted current pixel value of high resolution down-scaled image. It should be noted that according to formula (4), the strict linear relation between  $\epsilon$  and  $T$  is assumed.

The appropriate definition of the used high resolution data source, referred to here as  $\epsilon$ , is the most important issue in the utilized downscaling method. The better the description of local properties of the area the image of which is to be downscaled, the smaller the obtained error of transformation. The effective emissivity composite product values calculated based on several high resolution images were utilized as the HRK [27].

The PBIM allows for merging multiresolution 2D datasets retrieved from sensors. Note that in this approach, the simulated high resolution image retains the radiometric characteristics and spatial distribution of the original low resolution image. In particular, the average of the simulated high-resolution sub-pixel values is equal to the pixel value of the original low resolution image.

The PBIM method can be applied to any satellite imagery derived products - from a relatively low level, where pixel values are spectral bands of the images, to higher levels like LST or SST products.

Note also that in this approach to re-scaling of thermal products it is important that spatial data considered for processing must represent relatively flat areas, thus the low scale can be expressed as a simple aerial average of the LSTs at the high scale [28]. Also, the re-scaling methods have limitations for areas with high surface type diversity, which particularly refers to wetlands, water containers situated among sub pixel areas. Water surfaces have different emissivity and heat capacity properties and thus they significantly influence the model [29].

## 2.3 Proposed method of PBIM optimization

In the presented approach, as in the PBIM method, the  $\epsilon_{high}$  also plays a principal role, as it describes high resolution properties of an area corresponding to LST image to be downscaled. As mentioned,  $\epsilon_{high}$  is computed based on high resolution quasi-static data that describes thermal properties of an area. The choice on what should be the basis for the construction of  $\epsilon_{high}$  used for defining the rescaling transformation is somewhat arbitrary. The general rule



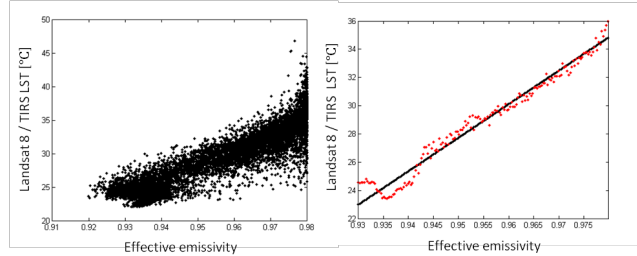
is that it should possibly describe the thermal properties of the surface in the best possible way - particularly the surface's susceptibility to absorb heat from shortwave radiation if the aim is to downscale day-time LST [30]. Also, what has been introduced in subsection 2.1,  $\epsilon_{high}$  is considered to be quasi-static and much easier to be retrieved than data to be downscaled [31]. Note also that images used to construct composite data must be registered in similar vegetation and weather conditions [32]. In our approach, we have taken under consideration the summer period of the years of 2013 and 2014. The FVC and subsequently the effective emissivity  $\epsilon$  have been calculated on the basis of the normalized differential vegetation index (NDVI) using the formulae (20) and (21) from subsection 3.2.

What is more, as mentioned in the previous section, the PBIM method relies on a relatively simple assumption that  $T_{high}$  depends linearly on the respective values (eq. 4). It can be observed that this is not always the case [33]. For instance, Fig. 2 presents the plot of effective emissivity from Landsat 8 OLI vs. corresponding values of LST from Landsat 8 TIRS for the investigated Pomerania region in Northern Poland (for details on data processing, and specifically on effective emissivity and LST calculating from Landsat 8 imagery – see section 3). The content of Fig. 2 is in general in line with the known observations of the “triangle” character of the VI – LST dependence. Fig. 2b shows the relation between effective emissivity values, namely, the central values of particular small ranges of effective emissivity, and LST values averaged for groups of pixels corresponding to those effective emissivity small ranges (red points). It is able to be seen from the figures that the relation between effective emissivity and LST tends not to be linear. The line of fit (corresponding to all data presented in Fig. 2a, not only to averaged data from Fig. 2b) is shown in Fig. 2b by black dots. It is visible that it cannot be used as a satisfactory approximation of  $\epsilon_{high}$  – LST dependence.

To take into account the non-linear dependence between the biophysical properties of the surface in the LST downsampling, the authors propose the following inverse downscaling approach ( $DS_{opt}$ ). We assume that there exists a dependence between effective emissivity and LST expressed as

$$LST_{high} = f(\epsilon_{high}), \quad (5)$$

where  $f(\cdot)$  need not to be linear (and does not have to be monotonic as well), and may be estimated for instance as the red plot in Fig. 2. Combining (2) and (5), and naming



(a)

(b)

**Figure 2:** LST/effective emissivity scatter plot for considered area (a). Right picture (b) represents effective emissivity and LST dependence for considered region: red plot vs. LST value represents averaged for groups of pixels corresponding to small ranges of effective emissivity. Black plot is a linear approximation of effective emissivity and LST dependence.

PV explicitly as LST, yields:

$$LST_{low} = \sum_{n=1}^N f(\epsilon_{high}^{(n)}) \frac{S_n}{N} \quad (6)$$

for a given low scale pixel. The form of  $f(\cdot)$  is generally unknown for a given terrain, but assuming that it is stable for the entire scene and applying (6) to each low scale pixel, we may express the problem as a system of linear equations. For this purpose, let us calculate the histogram  $[h_1, h_2, \dots, h_K]$  of  $\epsilon_{high}$  (where  $h_k, k = 1, \dots, K$  is the percentage of high scale pixels whose  $\epsilon_{eff}$  value belongs to a given range) for each low scale pixel, using always the same  $\epsilon_{eff}$  minimum/maximum values and the same number of bars  $K$ . Then, if we express  $f(\cdot)$  as a vector of values (weights)  $[w_1, w_2, \dots, w_K]$  corresponding to the central values of  $\epsilon_{eff}$  ranges used in calculating the histogram, and assuming that the single pixel area  $s_n$  is constant, we may write (6) as

$$LST_{low\ m} = \sum_{k=1}^K h_{mk} \cdot w_k \quad (7)$$

where  $m$  is the number of a “coarse” pixel in a scene ( $m = 1, \dots, M$ ). The system of  $M$  equations (7) may be also written in a matrix form:

$$LST_{low} = \mathbf{H} \cdot \mathbf{w} \quad (8)$$

and may be shown as a diagram – Fig. ??.

Referring to (7) and (8), each row in  $\mathbf{H}$  matrix represents information on thermal properties of terrain within a certain pixel of low resolution image (Fig. 3). Row values of  $\mathbf{H}$  represent histogram values calculated using a corresponding set of  $N$  pixel values of  $\epsilon_{eff}$  from high resolution image (in reality, usually less than  $N$  pixel values is used for a given coarse pixel, due to cloud presence or other

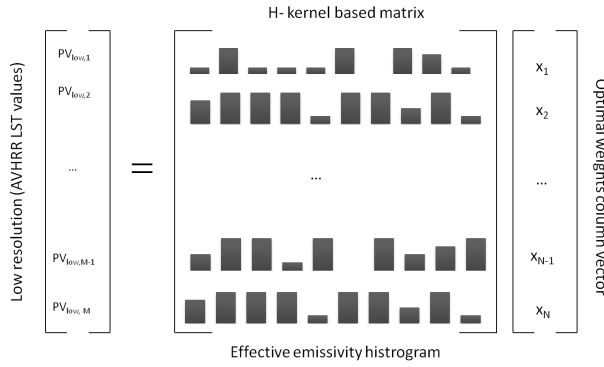


**Figure 3:** Diagram of matrix equation representing dependence between high and low resolution datasets

limitations in high scale data from which  $\epsilon_{high}$  has been derived).  $LST_{low}$  is a column vector containing low resolution image  $LST$  values and  $\mathbf{w}$  is the vector of weights to be found. Having two data sources ( $LST$  in a coarse scale and  $\epsilon_{high}$  in a fine scale) which fulfil the conditions stated above, for the whole scene a set of  $M$  equations with  $K$  variables is obtained.

Finally, as  $w_k$  values express the  $LST$  themselves, after finding them with use of the method described in the next subsection, the  $LST_{high}$  may be estimated directly as  $w_k$  corresponding to a given  $\epsilon_{high}$  value, or with the application of some kind of interpolation of  $\mathbf{w}$  values.

## 2.4 Finding an optimal solution

Now our task is to estimate  $\mathbf{w}$  having given  $LST_{low}$  and  $\mathbf{H}$ . Let us denote the observation vector  $LST_{low}$  as  $\mathbf{y}$  and the searched vector of parameters  $\mathbf{w}$  as  $\mathbf{x}$ , and include the vector  $\mathbf{v}$  of bias which is always present in a real measurement situation:

$$\mathbf{y} = \mathbf{H} \cdot \mathbf{x} + \mathbf{v}. \quad (9)$$

Estimation of  $\mathbf{x}$  having known  $\mathbf{H}$  and measured  $\mathbf{y}$  biased by unknown  $\mathbf{v}$  is a typical linear inverse problem [34]. Unfortunately, in reality we usually have to take into account that the postulated model does not describe the relation between  $\mathbf{x}$  and  $\mathbf{y}$  perfectly, e.g. it is linear only in approximation, or the assumed values in  $\mathbf{H}$  are not fully correct, or the assumed number of independent variables (the number of  $\mathbf{x}$  elements) is not correct. Moreover, the  $K$  and  $M$  values are not equal and thus  $\mathbf{H}$  matrix is not invertible. Thus, one of the possible ways to obtain the solution in such a situation is to estimate  $\mathbf{x}$  in a sense of least squares, i.e. by minimizing the  $\|\mathbf{H}\mathbf{x} - \mathbf{b}\|^2$  where  $\|\cdot\|^2$  is

the Euclidean norm. Estimate  $\hat{\mathbf{x}}$  may be then calculated as:

$$\hat{\mathbf{x}} = (\mathbf{H}^T \mathbf{H})^{-1} \mathbf{H}^T \mathbf{y} \quad (10)$$

if the  $\mathbf{H}^T \mathbf{H}$  matrix is not singular. In such a case, a regularization term is introduced to provide the existence of the solution, changing (10) to:

$$\hat{\mathbf{x}} = \mathbf{x}_0 + (\mathbf{H}^T \mathbf{H} + \mathbf{\Gamma})^{-1} (\mathbf{H}^T (\mathbf{y} - \mathbf{H}\mathbf{x}_0)) \quad (11)$$

where  $\mathbf{\Gamma}$  is a suitably chosen Tikhonov matrix [35-38] and  $\mathbf{x}_0$  is the expected solution calculated from the PBIM method. We used the simple form of  $\mathbf{\Gamma} = \lambda \mathbf{I}$ , where  $\mathbf{I}$  is the identity matrix and the  $\lambda$  value was found using the near-optimal parameter calculation of singular value decomposition method proposed by O-Leary [34].

The solution  $\hat{\mathbf{x}}$  is the optimal vector that minimizes the error of reconstruction of simulated high resolution image based on low resolution AVHRR imagery and utilized HRK that is stored in  $\mathbf{H}$  matrix.

At the last step of the proposed approach, the image is reconstructed to high resolution using optimal weights stored in  $\hat{\mathbf{x}}$ . Reconstruction is performed from  $\hat{\mathbf{x}}$  vector using local low resolution  $LST$  correction, denoted as  $DS_{opt}$ :

$$T(i, j)_{high} = \hat{\mathbf{x}} (H(\epsilon_{high}(i, j))) \frac{LST(\hat{i}, \hat{j})_{low}}{LST_{mean}}, \quad (12)$$

where:

- $(\hat{i}, \hat{j})$  denotes low resolution pixel coordinates that correspond to high resolution  $(i, j)$  coordinates,
- $\epsilon_{high}$  - is the effective emissivity.

## 3 Experimental setup

### 3.1 The experiment scheme and data flow

In order to compare the results obtained using the proposed approach with other existing solutions, we used two basic types of datasets: AVHRR and Landsat 8, registered at possibly the same time. Then, we assumed that AVHRR  $LST$  is a low spatial resolution (1.1 km) input data that is downscaled to higher resolution (100 m) and we treat Landsat 8  $LST$  product as a kind of proxy validation dataset.

In this case, the effective emissivity, as the static high resolution data to be merged with low resolution image, was retrieved from a composition of two Landsat 8 images registered on 2013-08-05 at 09:45:37 UTC (scene center time) and on 2014-07-23 at 09:43:29 UTC (scene center time). For both of the scenes, fractional conditions for the

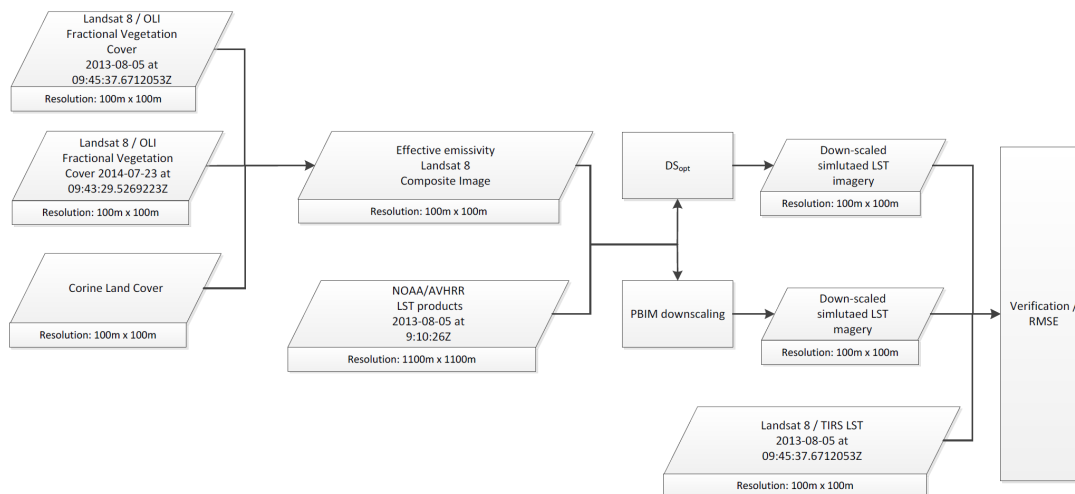


Figure 4: Overall diagram of data processing flow and verification

analyzed area are similar (middle of the summer) and repeatable. The Metop-B/AVHRR3 imagery was registered on 2013.08.05 on 9:10:26 UTC.

The overview diagram of processing and validation strategy of the proposed approach is presented in Fig. 4. After creating the composite FVC high resolution image from two Landsat 8 scenes, it was used along with the AVHRR low resolution LST image as an input to our downscaling procedure. Also, for comparison of the results, the PBIM downscaling was applied for the same data. At the end, a comparison of the down-scaling results, obtained both by  $DS_{opt}$  and PBIM with the high resolution Landsat 8 LST data, was performed.

It should be noted that for Landsat 8, in the climatic zone of the considered region several requirements need to be fulfilled to provide the appropriate analysis. The acquisition should be made under clean sky conditions in order not to interfere with the values registered in thermal and visible channels. The presence of clouds, aerosols, and diverse spatial distribution of water vapor content highly disturbs the process of acquisition. Also, note that Landsat 8 was launched in 2010 and together with a long revisit time (16 days), it highly reduces the number of available acquired imageries where all conditions stated above can be met.

We also performed accurate geometric calibration of both data sources to provide a unified reference system and cover the same areas of analysis. Data from both sources were reprojected to UTM zone 34 projection where the imageries cover area from 271872 to 434655 easting and 6004014 to 6092171 northing based on WGS 84 ellipsoid. The whole area covers 14,256 km<sup>2</sup>, in which land consists of about 51% of the data. The height of the terrain is not

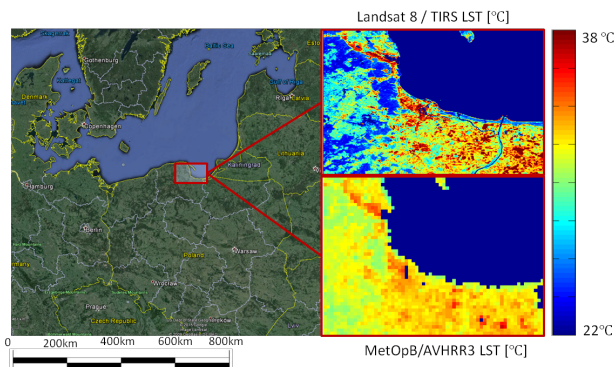


Figure 5: On the left: the map depicting the location of the area of interest – the Gulf of Gdańsk, South Baltic, Poland (source: Google Earth), on the right: LST maps calculated from both sensors – Landsat 8/TIRS (top-right) and MetOpB/AVHRR3 (bottom-right). Blue pixels in the upper and the lower right images represent sea or cloud areas that were masked out of the analysis.

moderately diverse as most of it is covered by flat areas or small hills. Diverse vegetation conditions of the urban areas of Gdańsk, Sopot and Gdynia municipality (Tricity), and green areas (forests, farmlands) located nearby, cause the NDVI to vary from approx. 0.12 to 0.67.

Fig. 5 presents the map of the location of the area of interest: the land at the Gulf of Gdańsk, Southern Baltic Sea in Poland, along with LST maps calculated using imageries from both sensors – high resolution Landsat 8 and low resolution MetOpB/AVHRR.

### 3.2 LST estimation

In the study, we selected MetOp-B/AVHRR3 imageries as the source of low resolution data to be downscaled and Landsat 8/TIRS LST as a validation dataset.

5 The set of NOAA and MetOp satellites utilizes the AVHRR radiation-detection moderate resolution remote imager dedicated to land and atmosphere. Due to quite a large number of currently operating NOAA and MetOp satellites, the AVHRR sensor is characterized by a relatively high time resolution (the revisit time for the respective region is approx. 2-3 hours). Tab. 1 presents the characteristics of AVHRR channels according to NOAA KLM User's Guide.

As it is known, LST estimation requires emissivity correction [39–42]. Therefore, during this process we calculate the average emissivity for 4<sup>th</sup> and 5<sup>th</sup> AVHRR channel, denoted as  $\epsilon_{AVHRR}$  and the difference of these channels' emissivity  $\Delta\epsilon_{AVHRR}$ . The calculation process was different for several NDVI ranges. Namely, for  $NDVI < 0.2$  the pixel is considered to be bare soil, then:

$$\begin{aligned}\epsilon_{AVHRR} &= 0.98 - 0.42 * R1, \\ \Delta\epsilon_{AVHRR} &= 0.003 - 0.029 * R1,\end{aligned}\quad (13)$$

where  $R1$  is AVHRR channel 1 reflectance.

Pixels with  $0.2 < NDVI < 0.5$  are considered to be partly vegetated and the  $\epsilon_{AVHRR}$  and  $\Delta\epsilon_{AVHRR}$  are calculated using the following formulae:

$$\epsilon_{AVHRR} = 0.971 - 0.018 P, \quad \Delta\epsilon_{AVHRR} = 0.006(1 - P),\quad (14)$$

where

$$P = \frac{(NDVI - 0.2)^2}{0.09}.\quad (15)$$

For  $NDVI > 0.5$  pixel is considered to be full vegetation and  $\epsilon_{AVHRR}$  and  $\Delta\epsilon_{AVHRR}$  is fixed as:

$$\epsilon_{AVHRR} = 0.93, \quad \Delta\epsilon_{AVHRR} = 0.\quad (16)$$

15 The validation dataset was retrieved from the Landsat 8 satellite, which images the entire Earth every 16 days in an 8-day offset from Landsat 7. Landsat 8 carries two instruments: the Operational Land Imager (OLI) sensor that includes refined heritage bands, along with three new bands with respect to Landsat 7 [43] a deep blue band for coastal/aerosol studies, a shortwave infrared band for cirrus detection, and a Quality Assessment band. The Thermal Infrared Sensor (TIRS) provides two thermal bands. Both these sensors provide improved signal-to-noise radiometric performance quantized over a 12-bit dynamic

range. The improved signal to noise performance of Landsat 8 enables better characterization of the land cover state and conditions. Products are delivered as 16-bit images (scaled to 55,000 grey levels). Table 2 presents the characteristics of Landsat 8 channels. 30

The LST from Landsat 8 imagery was calculated by applying the split window technique algorithm that uses two thermal bands located in the atmospheric window between 10 and 12  $\mu\text{m}$ . Then, we applied radiometric calibration procedure for Landsat 8 data using metadata of the provided imagery and used expansion of the Planck equation according to (17) for TIRS data. Spectral radiances delivered in Landsat datasets were converted into satellite brightness temperature using the following relationship [44, 45]:

$$T_{Bi} = \frac{K_2}{\ln\left(\frac{K_1}{TOA_i} + 1\right)}\quad (17)$$

where:

$K_1$  - band specific thermal conversion coefficient delivered with Landsat 8 imagery metadata files, namely  $K_1 = 774.89$  for channel 10 and 440.89 for channel 11  $\left[\frac{W}{m^2 \text{ ster } \mu\text{m}}\right]$ ,

$K_2$  - band specific thermal conversion coefficient delivered with Landsat 8 imagery metadata files, namely  $K_2 = 1321.08$  for channel 10 and 1201.14 for channel 11  $\left[\frac{W}{m^2 \text{ ster } \mu\text{m}}\right]$ .

$TOA_i$  - top of the atmosphere spectral radiance  $\left[\frac{W}{m^2 \text{ ster } \mu\text{m}}\right]$  registered for  $i$ -th thermal channel of Landsat 8 TIRS. 40

Landsat 8 LST emissivity correction, denoted as  $\epsilon_{TIRS}$ , was performed according to a procedure proposed by Skokovic et al. [46], Shaouhua Zhao et al. [47], according to the values presented in the Tab. 3, with use of the Corine Land Cover database and FVC data, in order to distinguish 45 urban and non-urban area.

The split window technique (SWT), utilizing the thermal channels of AVHRR3 and TIRS, has been used here for LST calculation. This is a relatively simple and robust method of retrieving LST estimation for large or regional scale applications. Its main property is that it removes atmospheric fluctuations, taking advantage of the fact that radiation absorption differs in particular wavelengths of electromagnetic spectra. Consequently, the TIRS and AVHRR LST images were corrected pixel by pixel for emissivity and water vapor content, according to Jimenez-Munoz [48–51] with values of  $c_0$ - $c_6$  (Tab. 4) according to the following formula:

$$\begin{aligned}LST &= T_i + c_1 \cdot (T_i - T_j) + c_2 \cdot (T_i - T_j)^2 \\ &\quad + c_0 + (c_3 + c_4 W) (1 - \hat{\epsilon}) + (c_5 + c_6 W) \Delta\epsilon,\end{aligned}\quad (18)$$





**Table 1:** Characteristics of AVHRR spectral channels

Channel Number	Resolution at Nadir	Wavelength ( $\mu\text{m}$ )	Typical Use
1	1.09 km	0.58 - 0.68	Daytime cloud and surface mapping
2	1.09 km	0.725 - 1.00	Land-water boundaries
3A	1.09 km	1.58 - 1.64	Snow and ice detection
3B	1.09 km	3.55 - 3.93	Night cloud mapping, sea and land surface temperature
4	1.09 km	10.30 - 11.30	Night cloud mapping, sea and land surface temperature
5	1.09 km	11.50 - 12.50	Sea and land surface temperature
REVISIT TIME: 8 per day			

**Table 2:** Characteristics of Landsat 8 spectral channels

Channel Number	Resolution at Nadir	Wavelength ( $\mu\text{m}$ )	Description/Typical Use
1	30 m	0.43 - 0.45	Coastal aerosol
2	30 m	0.45 - 0.51	Visible - blue
3	30 m	0.53 - 0.59	Visible green
4	30 m	0.64 - 0.67	Visible - red
5	30 m	0.85 - 0.88	Near infrared (NIR)
6	30 m	1.57 - 1.65	SWIR 1
7	30 m	2.11 - 2.29	SWIR 2
8	30 m	0.50 - 0.68	Panchromatic visible
9	30 m	1.36 - 1.38	Cirrus detection
10	100 m	10.60 - 11.19	Night cloud mapping, sea and land surface temperature
11	100 m	11.50 - 12.51	Sea and land surface temperature
REVISIT TIME: 16 days			

**Table 3:** Emissivity values for urban and non-urban areas for TIR bands

Emissivity	Band 10	Band 11
Land surface emissivity of urban area	0.971	0.977
Land surface emissivity of non - urban area	0.987	0.989

where  $W$  is a water vapor content retrieved from an external database [50–54],  $T_i$  and  $T_j$  are thermal channels of AVHRR ( $i = 4$  and  $j = 5$ ) and TIRS ( $i = 10$  and  $j = 11$ ) respectively,  $\hat{\epsilon}$  is the average emissivity for thermal channels of AVHRR3 and TIRS, respectively ( $\epsilon_{AVHRR}$  and  $\epsilon_{TIRS}$ ) and  $\Delta\epsilon$  is the emissivity difference between the thermal channels of AVHRR3 and TIRS.

With the above consideration in mind, in our methodology we proposed the following approach:

- 10 – we applied the split window technique for MetopB/AVHRR3 and for Landsat 8 TIRS,

- in both algorithms we used the surface emissivity and water vapor content correction approach.

Effective emissivity  $\epsilon$  computation was based on high resolution NDVI data over the respective region. The maximum NDVI ( $NDVI_{max}$ ) and the minimum NDVI ( $NDVI_{min}$ ) values for the study area were determined, which were further used for computing the fractional vegetation cover (FVC) [57, 58]:

$$FVC = \left( \frac{NDVI - NDVI_{min}}{NDVI_{max} - NDVI_{min}} \right)^2 \quad (19)$$



**Table 4:** Effective wavelengths for thermal channels used in SW technique and equation coefficients applied for LST estimation procedure for AVHRR and OLI

Platform/ sensor	$\lambda_i - \lambda_j$	$c_0$ [K]	$c_1$ [-]	$c_2$ [K <sup>-1</sup> ]	$c_3$ [K]	$c_4$ [K cm <sup>2</sup> g <sup>-1</sup> ]	$c_5$ [K]	$c_6$ [K cm <sup>2</sup> g <sup>-1</sup> ]
METOP B/ AVHRR3	10.82-11.97	-0.045	1.733	0.307	44.3	0.61	-150	18.7
Landsat 8/ TIRS	10.8-12	-0.268	1.378	0.183	54.3-2.238	-129.2	16.4	

and the effective emissivity  $\epsilon$  as:

$$\epsilon = 0.98(1 - FVC) + 0.93 FVC. \quad (20)$$

## 4 Results

### 4.1 Comparison of LST downscaling results for the entire scene

In this subsection we present the results obtained using the proposed optimized downscaling process of LST. We compared the results obtained by  $DS_{opt}$  with the PBIM method of downscaling in global (i.e. for the entire scene Fig. 6, and using a more detailed analysis in Fig. 7) and local scale (i.e. for the locations along the two selected transect lines within the investigated land area, Fig. 8, 9 and 10) using objective criteria, namely, the root mean squared error (RMSE) and the Pearson correlation coefficient (R). Pixels representing either clouds or sea on any of the images were masked during the analysis so their values did not interfere with the overall process of error minimization.

We compared the obtained downscaled high resolution image to LST calculated from Landsat 8 image acquired on 13 August 2013. The  $RMSE$  between Landsat 8 LST and downscaled image using  $DS_{opt}$  was  $2.255^\circ\text{C}$  with correlation coefficient  $R$  equal to 0.828 and  $Bias = 0.557^\circ\text{C}$ . It shows a significant improvement in comparison to the PBIM method, where we obtained  $RMSE = 2.832^\circ\text{C}$ ,  $R = 0.775$  and  $Bias = 0.997^\circ\text{C}$ .

The analysis of spatial distribution images shows that the results obtained by  $DS_{opt}$  algorithm better represent thermal characteristics for the analyzed area and are visually closer to the original Landsat 8 LST image than the image obtained using the PBIM method (Fig. 6). Specifically, it can be observed that the influence of local surface high resolution characteristics is reflected in  $DS_{opt}$  rather than local LST retrieved from AVHRR observations. What is more, as in the PBIM, the  $LST_{low}$  term is directly used in the formula and strongly influences the obtained  $LST_{high}$

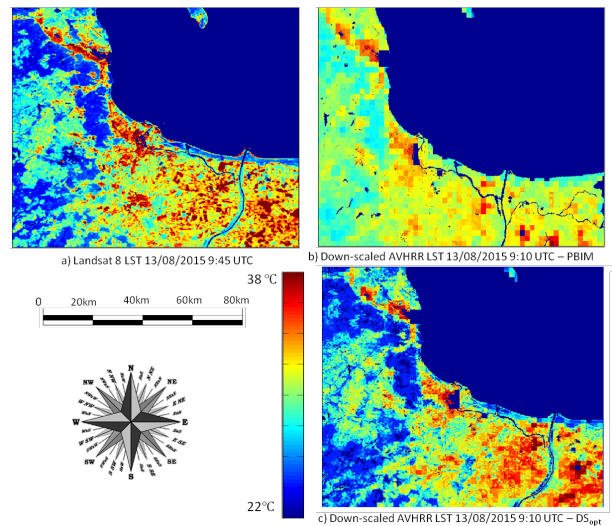


**Figure 6:** Comparison of downscaling results for the investigated area: top-left: LST calculated from Landsat 8 image, top-right: LST downscaled from AVHRR using PBIM method, bottom-right: LST downscaled from AVHRR using  $DS_{opt}$  method

value, it results in the appearance of coarse resolution artifacts in the downscaled product (Fig. 6b). This effect does not occur in the  $DS_{opt}$  result case. In Fig. 7 we presented the scatter plot of this case.

### 4.2 Detailed analysis of the retrieved results

In many cases, for instance for small areas where we deal with high diversity of surface conditions, obtaining the local accurateness of the applied downscaling is even more important. For this purpose, we took under consideration two relatively small sub-areas defined as narrow strips of land situated along selected “cross section” lines, in order to verify how the algorithm manages with diverse heterogeneous conditions (Fig. 8).

The first line starts from the West, at point A located at  $53.9356^\circ\text{N}$ ,  $17.6832^\circ\text{E}$ , which is situated in the suburbs of the Tricity area. Then, the line transects through the Tricity Landscape Park and ends in the urban area of the Tricity

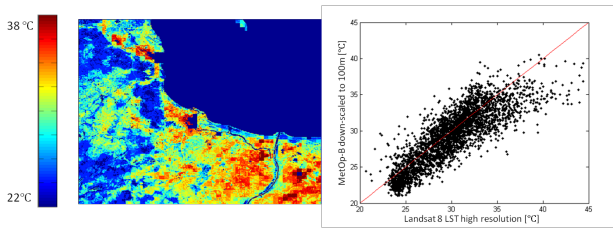


**Figure 7:** The obtained downscaled to high resolution AVHRR LST image and scatter plot (every 100<sup>th</sup> point) of Landsat 8 LST and downscaled AVHRR LST (right) using  $DS_{opt}$ . Red line in right image represents “1:1” line. Correlation coefficient and root mean squared error (RMSE) were:  $R=0.828$  and  $RMSE=2.255^{\circ}C$ , respectively.

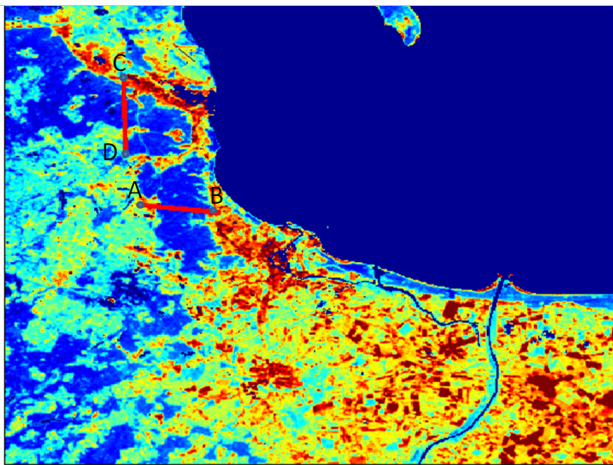


**Figure 8:** Landsat LST image with marked two transect lines defining the small subareas selected for detailed analysis of the downsampling results. The first line (AB) starts from suburban areas of the Tricity municipality (A), passes through a vegetated area of the Tricity Landscape Park and ends in the Tricity municipal area near the border between Gdańsk and Sopot (B). The second transect starts from the suburban area of Gdynia (C), passes through forest areas and ends in the center of Gdynia city (D).

municipality (Gdańsk-Oliva district) - point B ( $53.9309^{\circ}N$   $17.8077^{\circ}E$ ). The length of the line is 6 km and it transects through low as well as very high vegetated areas, so the thermal conditions along this transect are significantly diversified.

The second line starts from suburban area of Gdynia (point C –  $54.045^{\circ}N$ ,  $17.6513^{\circ}E$ ), passes through forest areas and ends in the center of Gdynia city (point D –  $53.9544^{\circ}N$ ,  $17.6601^{\circ}E$ ). The diversity of thermal conditions for the area along the second transect is quite similar to that in the case of the first line.

Afterwards we performed analysis of the obtained results along selected transects from four datasets, namely:

- LST calculated from Landsat 8 TIRS dataset (validation dataset),

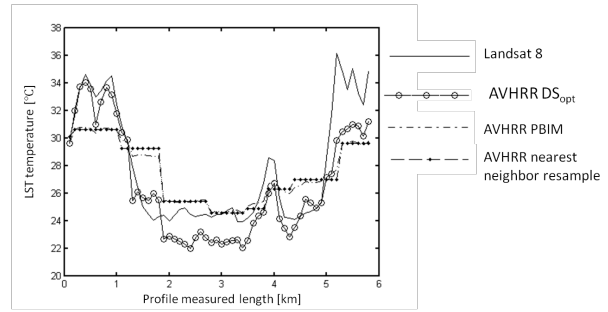


**Figure 9:** Comparison of LST high resolution data with respect to AB transect line: Landsat 8 LST, AVHRR LST downsampled by  $DS_{opt}$  method, AVHRR LST downsampled by PBIM method and AVHRR LST downsampled by nearest neighbor technique

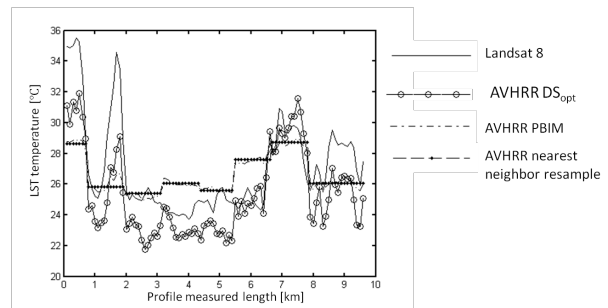


**Figure 10:** Comparison of LST high resolution data with respect to CD transect line: Landsat 8, AVHRR  $DS_{opt}$  downsampled by the proposed method, AVHRR downsampled by the PBIM method (AVHRR PBIM) and AVHRR resampled to LANDSAT 8 resolution using nearest neighbor technique

- AVHRR LST image downsampled using the proposed  $DS_{opt}$  method,
- AVHRR LST image downsampled using the PBIM method,
- AVHRR LST image downsampled transformed (resampled) to high resolution by simple nearest neighbor method.

Plotted LST high resolution values taken from particular datasets along the AB and CD transect, respectively are presented in Fig. 9 and 10. Tables 5 and 6 contain the comparison of the correlation coefficient and RMSE between Landsat 8 LST and the results retrieved by different methods of AVHRR LST downscaling:  $DS_{opt}$  proposed by the authors, PBIM, and nearest neighbor for AB and CD transect, respectively.

For this relatively small area, the above results show that the optimization method presented in  $DS_{opt}$  algorithm yields significantly better results than other approaches. Note that the aim of using the inverse problem algorithm is to minimize the downscaling error in a global, i.e. the



**Table 5:** Comparison of the results obtained by different downsampling methods for the subarea indicated by AB transect

Downsampling method	Correlation coefficient $R$ with respect to Landsat 8 LST	$RMSE$ [ $^{\circ}C$ ] with respect to Landsat 8 LST	$BIAS$ [ $^{\circ}C$ ] with respect to Landsat 8 LST
$DS_{opt}$	0.9334	2.0042	1.3529
PBIM	0.8207	2.6851	0.3939
Nearest neighbor	0.7544	2.8757	0.4034

**Table 6:** Comparison of the results obtained by different downsampling methods for the subarea indicated by CD transect

Downsampling method	Correlation coefficient $R$ with respect to Landsat 8 LST	$RMSE$ [ $^{\circ}C$ ] with respect to Landsat 8 LST	$BIAS$ [ $^{\circ}C$ ] with respect to Landsat 8 LST
$DS_{opt}$	0.842	2.3927	1.7932
PBIM	0.6038	2.5262	0.4812
Nearest neighbor	0.5101	2.659	0.4581

entire imagery scale, so results corresponding to local sub-datasets do not always have to be better than when using other methods. However, this case shows that data obtained by the  $DS_{opt}$  fits the original Landsat 8 LST the best, which serves here as a kind of proxy verification tool.

As shown above, the obtained downscaled products retain radiometric characteristics of original images for the whole imagery, however, for subdatasets the BIAS results suggest that some deviation from this rule occurs. Moreover, the correlation coefficients and RMSE indicate that  $DS_{opt}$  technique yields results closer to the original high-resolution spatial pattern than the PBIM method. A more detailed investigation of the selected transect cross sections of the analyzed area indicates that also for small sub-datasets the usage of  $DS_{opt}$  is justified as the RMSE error is reduced from  $2.6851^{\circ}C$  for the PBIM case to  $2.0042^{\circ}C$  for AB transect and from  $2.5262^{\circ}C$  to  $1.5401^{\circ}C$  for CD transect. The improvement of the proposed methodology is further verified by correlation between downscaled products and time-coincident Landsat 8 imagery. Specifically, the correlation coefficient increases from 0.8207 to 0.9212 in the case of AB, and from 0.6038 to 0.8953 in the case of CD transect.

### 4.3 Optimized downscaling for local scale

In the previous subsection, we have examined and evaluated the results of downscaling using the inverse technique for the whole scene imagery and for particular transect sub-datasets. We have shown that the proposed optimization technique yields better results in comparison with the direct approach. In this section, we have taken un-

der consideration three sub-datasets of the whole scene, which differ between each other in terms of vegetation and surface conditions, and we have verified how our approach functions in such cases. The cases taken under consideration are as follows:

Case 1 - area covering nearly  $300 \text{ km}^2$  of Gdynia municipality urban area and Tricity National Park bounded by  $53.7451^{\circ}N$ ,  $18.4904^{\circ}E$  (north-west) and  $53.5237^{\circ}N$ ,  $18.6786^{\circ}E$  (south-east) limits. This area is rather unique and is to large extent characterized by surface type heterogeneity typical for urban area. According to the Corine Land Cover database, 51% of the mentioned area is urban, while 49% is non-urban, high vegetation area of the Tricity National Park. The results obtained by PBIM and  $DS_{opt}$  methods for test case 1 are shown visually in Fig. 11. The quantitative results on the obtained correlation coefficient, the RMS error and the bias for this case are shown in Table 7.

Case 2 - area of the Stężycza Lake which is a part of the Pomeranian National Park that mainly comprise vegetated areas (forests and grasslands), which constitute 99% of the surface. The area is bounded by coordinates:  $53.5222^{\circ}N$ ,  $17.9436^{\circ}E$  (north-east) and  $53.3807^{\circ}N$ ,  $18.3026^{\circ}E$  (south-west). The results obtained by PBIM and  $DS_{opt}$  methods for test case 2 are shown visually in Fig. 12. The quantitative results on the obtained correlation coefficient, the RMS error and the bias for this case are shown in Table 8.

Case 3 - urban area of Gdańsk municipality, bounded by  $53.5281^{\circ}N$ ,  $18.5208^{\circ}E$  and  $53.3891^{\circ}N$ ,  $19.1395^{\circ}E$ , that mainly comprise urban areas (over 80% according to the Corine Land Cover database). The results obtained by



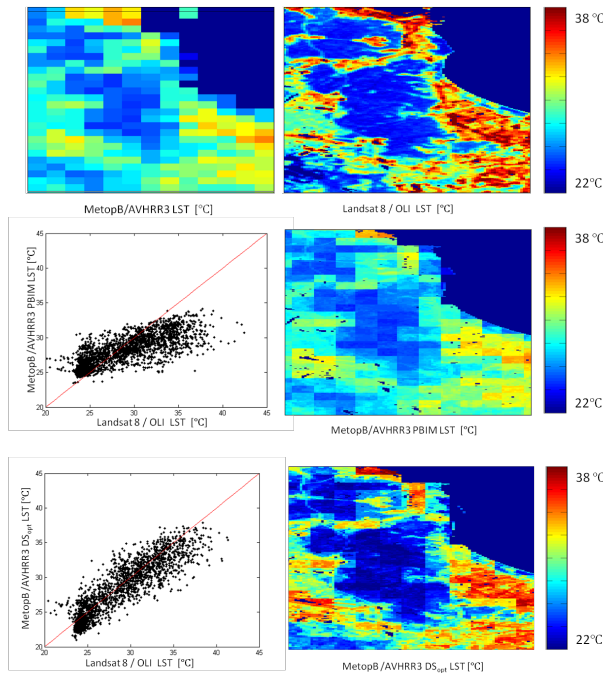


**Figure 11:** Scatterplot and visual presentation of the results retrieved by PBIM and  $DS_{opt}$  methods for local sub-dataset test case 1

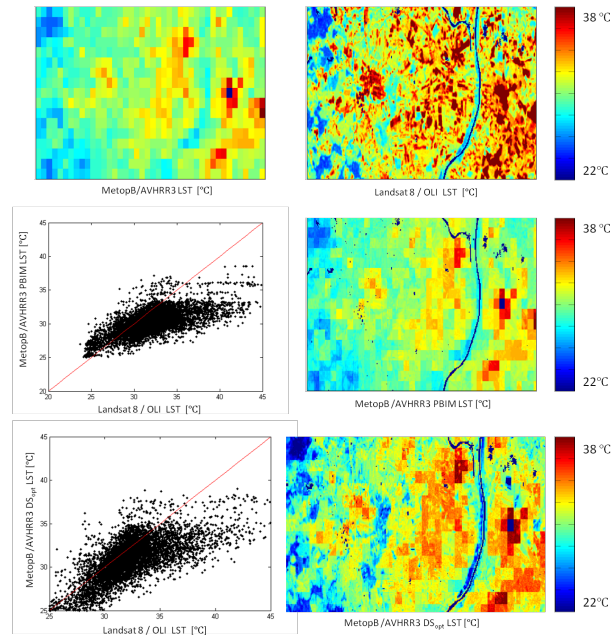


**Figure 13:** Scatterplot and visual presentation of the results retrieved by PBIM and  $DS_{opt}$  methods for local sub-dataset test case 3.

PBIM and  $DS_{opt}$  methods for test case 3 are shown visually in Fig. 13. The quantitative results on the obtained correlation coefficient, the RMS error and the bias for this case are shown in Table 9.

Tables 7-9 present analytical results obtained by the proposed optimization approach, PBIM method and original AVHRR3 data resampled using the nearest neighbor technique (presented in the third row) for cases 1-3. The second column of the tables represents the Pearson correlation coefficient, while the third represents the  $RMSE$  with respect to reference LST Landsat 8 OLI dataset. The last column shows  $BIAS$  between reference dataset and a result of downscaling products, in order to verify retention of radiometric properties of the results.

The results presented in these cases show that  $DS_{opt}$  method yields results closest to Landsat 8/TIRS validation dataset having overall lowest  $RMSE$  and highest correlation coefficient among the methods presented. This can be particularly observed for test case 1 (Tab. 7) when algorithm finds minimized error solution for a heterogeneous area, including high vegetation (low effective emissivity) and urban areas (high effective emissivity), yielding  $RMSE$  reduction up to 32% (for  $DS_{opt}$ ) and correlation increase from 0.7659 (for PBIM) to 0.8866 ( $DS_{opt}$ ). As this trend is also observed in cases 2 and 3 (Tab. 8 and Tab. 9, respectively), it may be concluded that the increase of the pro-

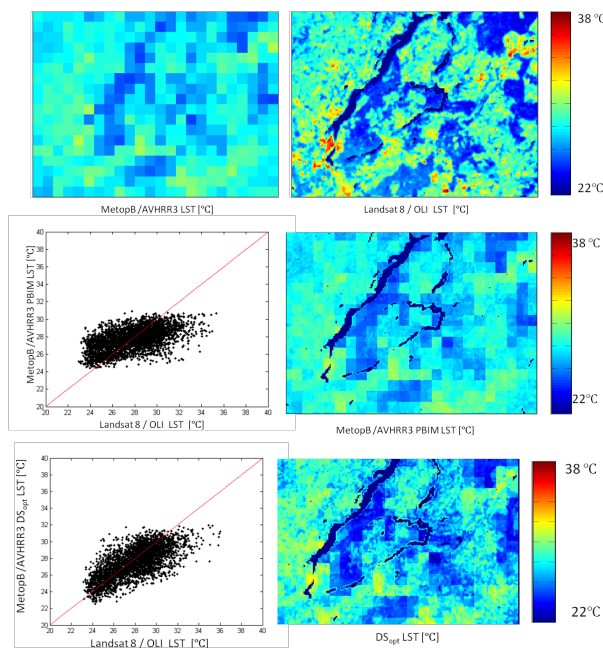


**Figure 12:** Scatterplot and visual presentation of the results retrieved by PBIM and  $DS_{opt}$  methods for local sub-dataset test case 2

**Table 7:** Results of downscaling using PBIM and  $DS_{opt}$  for local sub-dataset case 1

Downsampling method	Correlation coefficient $R$ with respect to Landsat 8 LST	$RMSE$ [ $^{\circ}C$ ] with respect to Landsat 8 LST	$BIAS$ [ $^{\circ}C$ ] with respect to Landsat 8 LST
$DS_{opt}$	0.8866	2.0513	0.5092
PBIM	0.7659	2.9984	0.7295
Nearest neighbor	0.7053	3.1898	0.7295

**Table 8:** Results of downscaling using PBIM and  $DS_{opt}$  for local sub-dataset case 2

Downsampling method	Correlation coefficient $R$ with respect to Landsat 8 LST	$RMSE$ [ $^{\circ}C$ ] with respect to Landsat 8 LST	$BIAS$ [ $^{\circ}C$ ] with respect to Landsat 8 LST
$DS_{opt}$	0.6991	1.6796	0.3998
PBIM	0.5587	1.8755	0.1742
Nearest neighbor	0.4741	1.9937	0.1742

**Table 9:** Results of downscaling using PBIM and  $DS_{opt}$  for local sub-dataset case 3

Downsampling method	Correlation coefficient $R$ with respect to Landsat 8 LST	$RMSE$ [ $^{\circ}C$ ] with respect to Landsat 8 LST	$BIAS$ [ $^{\circ}C$ ] with respect to Landsat 8 LST
$DS_{opt}$	0.7204	2.7159	1.4712
PBIM	0.6473	3.1649	1.8911
Nearest neighbor	0.5956	3.2609	1.8911

posed downscaling method performance is visible for local sub-datasets.

## 5 Conclusions

In the paper, the process of optimization of downscaling thermal products based on low resolution (AVHRR) imagery using the inverse technique approach was presented. The authors proposed a data processing model and method that transforms the downscaling process to inverse problem. We used Tikhonov regularization when finding an optimal solution to the defined problem and showed that our approach yields better results than the other approach, i.e. the PBIM direct method.

The proposed approach aims to find estimation of high resolution imagery by minimizing the global error of the downscaling process. Nevertheless, we showed by examples that apart from global optimization, the obtained results are also very good in local scale and can be used for relatively small areas – much smaller than the entire satellite imagery scene, depicting diverse surface conditions.

It should be pointed out that applying the inverse problem approach to the downscaling process is constrained by limitations and distortions. One of the main known difficulties regarding the satellite imagery processing in general is the appropriate atmospheric correction for cloud and aerosol presence and the need to remove the effects caused by atmospheric conditions. A standard model application for cloudy days can significantly decrease its quality as clouds and aerosols absorb radiation, thus making the precise effective emissivity and LST determination difficult to obtain. Hence, when the downscaling process described in this paper aims to minimize the global error and estimate the optimal weights vector, the presence of pixels not representing precise land surface conditions can perturb the entire result very strongly. In this sense, direct methods are more resistant to that type of effects.

Another aspect of the proposed methodology is the regularization parameter value. In many inverse problems, the estimation of the appropriate regularization parameter value is of a crucial importance. In our case, the optimal value was found by using near optimal parameter calculation methods based on singular value decomposition.



The kernel of the whole transformation process is the high resolution kernel matrix - it describes thermal properties of an area to be downscaled. The appropriate definition of HRK, its resolution as well as the kind of model describing the dependence of the LST on the quantity which is expressed by HRK values, determines the quality of the retrieved results. In the presented approach, we used fractional vegetation cover values to construct the HRK, but in general the HRK may be constructed from any spatial datasets that fulfill the conditions mentioned in section 2.

The proposed methodology that utilizes the inverse problem approach is a technique that can be applied to optimize the downscaling process and it can also be used in conjunction with other downscaling approaches and methods. The method is particularly suitable for cases where local biophysical conditions significantly influence the final characteristics of LST-VI relation. It is important to notice that the proposed methodology is self-adaptive in terms of technical implementation. The method constructs the high resolution kernel without human supervision, which means that applying it to regions with other climatic and meteorological conditions should be relatively straightforward. In particular, in cases where diverse vegetation conditions areas are analyzed, methods that find the minimum error solution are of considerable interest and are usually able to generate radiometric LST product that better depicts spatial distribution of LST.

## References

- [1] Arnfield A. J., Two decades of urban climate research: A review of turbulence, exchanges of energy and water, and the urban heat island. *International Journal of Climatology*, 2003, 23, 1-26, DOI: 10.1002/joc.859
- [2] Urbański J. A., Wochna A., Bubak I., Grzybowski W., Łukawska-Matuszewska K., Lacka M. et al., Application of Landsat 8 imagery to regional-scale assessment of lake water quality. *International Journal of Applied Earth Observation and Geoinformation*, 2016, 51, 28-36, DOI: 10.1016/j.jag.2016.04.004
- [3] Chybicki A., Łubniewski Z., Kulawiak M., Characterizing surface and air temperature in the Baltic Sea Coastal Area using remote sensing techniques. *Polish Maritime Research*, 2016, .3, 3-11, 2016, DOI: 10.1515/pomr-2016-0001
- [4] Merchant C. J., Matthiesen S., Rayner N. A., Remedios J. J., Jones P. D., Olesen F. et al., The surface temperatures of the earth: steps towards integrated understanding of variability and change, *Geosci. Instrumentation Methods Data Syst. Discuss.* 2013, 3, 305-345, DOI: 10.5194/gid-3-305-2013
- [5] Kustas W. P., Anderson M. C., Norman J. N., French A. N., Estimating subpixel surface temperatures and energy fluxes from the vegetation index-radiometric temperature relationship. *Remote Sensing of Environment*, 2003, 85, 429-440
- [6] Yang G., Puc R., Zhaoa C., Huang W., Wang J., Estimation of subpixel land surface temperature using an endmember index based technique: A case examination on ASTER and MODIS temperature products over a heterogeneous area. *Remote Sensing of Environment*, 2011, 115(5), 15, 1202-1219, DOI: 10.1016/j.rse.2011.01.004
- [7] Stathopoulou M., Cartalis C., Keramitsoglou I., Mapping micro-urban heat islands using NOAA/AVHRR images and CORINE Land Cover: An application to coastal cities of Greece. *International Journal of Remote Sensing*, 2004, 25, 2301-2316, DOI: 10.1080/01431160310001618725
- [8] Mitraka Z., Chrysoulakis N., Doxani G., Del Frate F., Berger M., Urban Surface Temperature Time Series Estimation at the Local Scale by Spatial-Spectral Unmixing of Satellite Observations. *Remote Sens.*, 2015, 7(4), 4139-4156, DOI: 10.3390/rs70404139
- [9] Bechtel B., Zakšek K., Hoshyaripour G., Downscaling land surface temperature in an urban area: A case study for Hamburg, Germany. *Remote Sens.*, 2012, 4, 3184-3200, DOI: 10.3390/rs4103184
- [10] Keramitsoglou I., Kiranoudis C. T., Weng Q. Downscaling geostationary land surface temperature imagery for urban analysis. *IEEE Geosci. Remote Sens. Lett.* 2013, 10, 1253-1257
- [11] Lewis H. G., Nixon M.S., Tatnall A. R. L., Brown M., Appropriate strategies for mapping land cover from satellite imagery, *Proceedings of the 25th Annual Conference of The Remote Sensing Society*, Cardiff, United Kingdom, 1999, pp. 717-724.
- [12] Lewis H. G., Brown M., Tatnall A. R. L., Incorporating uncertainty in land cover classification from remote sensing imagery. *Advanced Space Research A.R.L.*, 2000, 26(7), 1123-1126
- [13] Seetle J. J., Drake N. A., Linear mixing and the estimation of ground cover proportions. *International Journal of Remote Sensing*, 1997, 14(6), 1559-1177
- [14] Williamson H. D., Estimating sub-pixel components of a semi-arid woodland. *International Journal of Remote Sensing*, 1994, 15, 3303-3307
- [15] Atkinson P. M., Cutler M. E. J., Lewis H., Mapping sub-pixel proportional land cover with AVHRR imagery. *International Journal of Remote Sensing*, 1997, 188, 917-935
- [16] Mather P. M., Tso B., *Classification Methods for Remotely Sensed Data*. Taylor and Francis, 2001
- [17] Fisher P. F., Pathirana S., The evaluation of fuzzy memberships of land cover classes in the suburban zone. *Remote Sensing of Environment*, 1990, 34, 121-132
- [18] Foody G. M., Approaches for the production and evaluation of fuzzy land cover classifications from remotely-sensed data. *International Journal of Remote Sensing*, 1996, 17, 1317-1340
- [19] Xiong Xu, Yanfei Zhong, Adaptive Subpixel Mapping Based on a Multiagent System for Remote-Sensing Imagery. *IEEE Transactions on Geoscience and Remote Sensing*, 2014, 52, 2, 787-804
- [20] Guo L. J., Moore J. M., Pixel block intensity modulation: Adding spatial detail to TM band 6 thermal imagery. *International Journal of Remote Sensing*, 1998, 19(13), 2477-2491
- [21] Jiang L. S., Islam S., A methodology for estimation of surface evapotranspiration over large areas using remote sensing observations. *Geophysical Research Letters*, 1999, 26, DOI: 10.1029/1999GL006049
- [22] Jiang L. S., Islam S., Estimation of surface evaporation map over southern Great Plains using remote sensing data. *Water Resources Research*, 2001, 37, DOI: 10.1029/2000WR900255
- [23] Valipour M., Optimization of neural networks for precipitation



- analysis in a humid region to detect drought and wet year alarms. *Meteorological Applications*, 2016, 23(1), 91–100
- [24] Liang S., Validation and spatial scaling. In: Kong J. (Ed.), *Quantitative Remote Sensing of Land Surfaces*. Wiley & Sons, New Jersey, 2004, 431-471
- [25] Munechika C. K., Warnick J. S., Salvaggio C., Schott J. R., Resolution enhancement of multispectral image data to improve classification accuracy. *Photogrammetric Engineering and Remote Sensing*, 1993, 59, 67-72
- [26] Petropoulos G., Carlson T., Wooster M., Islam S., A Review of  $T_s/VI$  Remote Sensing Based Methods for the Retrieval of Land Surface Fluxes and Soil Surface Moisture Content. *Progress in Physical Geography*, 2009, 33(2), 224-250
- [27] Stathopoulou M., Cartalis C., Downscaling AVHRR land surface temperatures for improved surface urban heat island intensity estimation. *Remote Sensing of Environment*, 2009, 113, 2592-2605
- [28] Liu Y., Hiyama T., Yamaguchi Y., Scaling of land surface temperature using satellite data: A case examination on ASTER and MODIS products over a heterogeneous terrain area. *Remote Sensing of Environment*, 2006, 105, 115-128
- [29] Valipour M., Mohammad Ali Gholami Sefidkouhi, Mahmoud Raeini-Sarjaz, Selecting the best model to estimate potential evapotranspiration with respect to climate change and magnitudes of extreme events. *Agricultural Water Management*, 2017, 180(A), 50-60, <http://dx.doi.org/10.1016/j.agwat.2016.08.025>
- [30] Jiménez-Muñoz J. C., Sobrino J. A., A generalized single-channel method for retrieving land surface temperature from remote sensing data. *Journal of Geophysical Research*, 2003, 108(D22)
- [31] Hoerl A. E., Kennard R. W., Ridge regression: Biased estimation for nonorthogonal problems. *Technometrics*, 1992, 12, 55–67
- [32] Knight J. F., Lunetta R. S., Ediriwickrema J., Khorram S., Regional scale land cover characterization using MODIS-NDVI 250 m multi-temporal imagery: a phenology-based approach. *GI-Science Remote Sens.*, 2006, 43, 1-23
- [33] Stisen S., Sandholt I., Nørgaard A., Fensholt R., Jensen K. H., Combining the triangle method with thermal inertia to estimate regional evapotranspiration - Applied to MSG-SEVIRI data in the Senegal River basin. *Remote Sensing of Environment*, 2008, 112(3), 1242-1255
- [34] O’Leary D., Near optimal parameters for Tikhonov regularization and other regularization methods. *SIAM Journal on Scientific Computing*, 2001, 23(4), 1161-1171
- [35] Morozov V. A., On the solution of functional equations by the method of regularization. *Soviet Math. Dokl.*, 1996, 7, 414–417
- [36] Golub G., Heath M., Wahba G., Generalized cross-validation as a method for choosing a good ridge parameter. *Technometrics*, 1979, 21, 215–223
- [37] Hansen P. C., Analysis of discrete ill-posed problems by means of the L-curve. *SIAM Rev.*, 1992, 34, 561-580
- [38] Moody A. J. F., Lawless A. S., Pothast R. W. E., P. Van Leeuwen J., Nonlinear error dynamics for cycled data assimilation. Report no. MPS-2012-06, 2013
- [39] Li Z.L., Wu H., Wang N., Qiu S., Sobrino J. A., Wan Z. et al., Land surface emissivity retrieval from satellite data, *Int. J. Remote Sens.*, 2012, 34, 3084–3127
- [40] Sobrino J. A., Coll C., Caselles V., Atmospheric correction for land surface temperature using NOAA-11 AVHRR channels 4 and 5. *Remote Sensing of Environment*, 1991, 38, 19–34
- [41] Sobrino J. A., Li Z.L., Stoll P., Impact of the atmospheric transmittance and total water vapor content in the algorithms for estimating satellite sea surface temperatures. *IEEE Transactions on Geoscience and Remote Sensing*, 1993, 31, 946-952
- [42] Sobrino J. A., Li, M Z. L., Stoll P., Becker F., Improvements in the split-window technique for land surface temperature determination. *IEEE Transactions on Geoscience and Remote Sensing*, 1994, 32, 243-253
- [43] U.S. Geological Survey, The Landsat 8 Data User’s Handbook, <http://landsat.usgs.gov/l8handbook.php> (access on January 2016)
- [44] Schott J. R., Volchok W. J., Thematic Mapper thermal infrared calibration. *Photogrammetric Engineering and Remote Sensing*, 1985, 51, 1351–1357
- [45] Wukelic G. E., Gibbons D.E., Martucci L. M., Foote H. P., Radiometric calibration of Landsat Thematic Mapper Thermal Band. *Remote Sensing of Environment*, 1989, 28, 339–347
- [46] Skokovic D., Sobrino J. A., Jimenez-Munoz J. C., Soria G., Julien Y., Mattar C. et al., Calibration and Validation of Land Surface Temperature for Landsat 8 – TIRS Sensor. In: *Land Product Validation and Evolution*, ESA/ESRIN, Frascati (Italy), 2014, 6-9
- [47] Shaohua Zhao, Qiming Qin, Yonghui Yang, Yujiu Xiong and Guoyu Qiu, Comparison of two Split-Window Methods for Retrieving Land Surface Temperature from MODIS Data. *Journal of Earth Syst. Science*, 2009, 118, 4, 345- 353
- [48] Jimenez-Munoz J. C., Sobrino J. A., Split-window Coefficients for Land Surface Temperature Retrieval from Low-Resolution Thermal Infrared Sensors. *IEEE Geoscience and Remote Sensing Letters*, 2008, 5(4), 806-809
- [49] Jiménez-Muñoz J. C., Sobrino J. A., Skokovic D., Mattar C., Cristóbal J., Land Surface Temperature Retrieval Methods from Landsat-8 Thermal Infrared Sensor Data. *IEEE Geoscience and Remote Sensing Letters*, 2014, 11, 1840-1843
- [50] Shahid Latif M. D., Land Surface Temperature Retrieval of Landsat-8 Data Using Split Window Algorithm - A Case Study of Ranchi District. *International Journal of Engineering Development and Research*, 2014, 2(4), 3840-3849
- [51] Jiménez-Muñoz J.C., Sobrino J.A., A generalized single-channel method for retrieving land surface temperature from remote sensing data. *Journal of Geophysical Research*, 2008, 108, 4688–4695
- [52] Dubovik O., Holben B. N., Eck T. F., Smirnov A., Kaufman Y. J., King M. D. et al., Variability of absorption and optical properties of key aerosol types observed in worldwide locations. *J.Atm.Sci.*, 2002, 59, 590-608
- [53] Aires F., Chédin A., Scott N. A., Rossow W. B., A regularized neural net approach for retrieval of atmospheric and surface temperatures with the IASI instrument. *J. Appl. Meteorol.*, 2002, 41, 2, 144–159
- [54] Sobrino J. A., Raissouni N., Simarro J., Nerry F., Petitcolin F., Atmospheric Water Vapor Content over Land Surfaces Derived from the AVHRR Data: Application to the Iberian Peninsula. *IEEE Transactions on Geoscience and Remote Sensing*, 1999, 37, 3, 1425-1434
- [55] Michalakes J., Dudhia J., Gill D., Henderson T., Klemp J., Skamrock W. et al., The Weather Research and Forecast Model: Software Architecture and Performance. In: *Mozdzynski G. (Ed.), Proceedings of the 11<sup>th</sup> ECMWF Workshop on the Use of High Performance Computing in Meteorology*, Reading, 2004
- [56] Żróbek-Sokolnik A., Dynowski P., Stańczuk-Gatwiaczek M., Kryszk H., Kurowska K., Dudzińska M. et al., Application of ge-



- ographic information system tools in a broad natural science: Estimation and evaluation of Earth surface characteristics using numerical weather prediction and satellite imagery. *Nacjonalna Knijznica, Zagreb*, 2014, p.115
- 5 [57] Choudhury B. J., Ahmed N. U., Idso S. B., Reginato R. J., Daughtry C. S. T., Relations between evaporation coefficients and vegetation indices studied by model simulations. *Remote Sensing of Environment*, 1994, 50, 1-17
- [58] Gillies R. R., Carlson T. N., Thermal remote sensing of surface soil water content with partial vegetation cover for incorporation into climate models. *Journal of Applied Meteorology*, 1995, 34, 45-756